Article

Bacterial cell wall-specific nanomedicine for the elimination of *Staphylococcus aureus* and *Pseudomonas aeruginosa* through electron-mechanical intervention

Yanling You[1,2], Xu Yu[1,2], Junjie Jiang[3], Zhixin Chen[1,2,4], Ya-Xuan Zhu[4], Yihan Chen[1,2], Han Lin [1,2,4] ✉ & Jianlin Shi [1,2,4]

Personalized synergistic antibacterial agents against diverse bacterial strains are receiving increasing attention in combating antimicrobial resistance. However, the current research has been struggling to strike a balance between strain specificity and broad-spectrum bactericidal activity. Here, we propose a bacterial cell wall-specific antibacterial strategy based on an in situ engineered nanocomposite consisting of carbon substrate and decorated TiO_x dots, termed TiO_x@C. The fiber-like carbon substrate of TiO_x@C is able to penetrate the bacterial membrane of *Pseudomonas aeruginosa* (*P. aeruginosa*), but not that of *Staphylococcus aureus* (*S. aureus*) due to its thicker bacterial wall, thus achieving bacterial wall specificity. Furthermore, a series of experiments demonstrate the specific electro-mechanical co-sterilization effect of TiO_x@C. On the one hand, TiO_x@C can disrupt the electron transport chain and block the energy supply of *S. aureus*. On the other hand, TiO_x@C capable of destroying the membrane structure of *P. aeruginosa* could cause severe mechanical damage to *P. aeruginosa* as well as inducing oxidative stress and protein leakage. In vivo experiments demonstrate the efficacy of TiO_x@C in eliminating 97% of bacteria in wounds and promoting wound healing in wound-infected female mice. Overall, such a bacterial cell wall-specific nano-medicine presents a promising strategy for non-antibiotic treatments for bacterial diseases.

The emergence of antimicrobial resistance (AMR) in bacteria has posed a challenge to intractable infections[1]. Antibiotics and micro-organisms have combatted each other for nearly a century, in which bacteria have developed adaptive ability to evade the activity of many conventional antibiotics[2]. AMR bacteria bring a global crisis, increasing the morbidity and mortality of infected individuals and negatively impacting clinical outcomes in diverse populations[3]. In 2022, the WHO Global Report on Infection Prevention and Control identified 4.95 million deaths related to bacterial AMR worldwide in 2019[4]. There is an urgent need to tackle the progression of bacterial

[1]Shanghai Institute of Ceramics Chinese Academy of Sciences; Research Unit of Nanocatalytic Medicine in Specific Therapy for Serious Disease, Chinese Academy of Medical Sciences, Shanghai 200050, P. R. China. [2]Center of Materials Science and Optoelectronics Engineering, University of Chinese Academy of Sciences, Beijing 100049, P. R. China. [3]Shanghai Guanghua Hospital, Shanghai University of Traditional Chinese Medicine, Shanghai 200052, P. R. China. [4]Shanghai Tenth People's Hospital, Shanghai Frontiers Science Center of Nanocatalytic Medicine, School of Medicine, Tongji University, Shanghai 200331, P. R. China. ✉e-mail: linhan@mail.sic.ac.cn

AMR, which requires global comprehensive initiatives, including the rational use of antibiotics, stronger regulation, and the development of innovative 'outside of the box' therapeutics.

Therapeutics based on nanomaterials are promising tools for combating hard-to-treat bacterial infections, with the characteristic advantage of being able to evade existing mechanisms associated with acquired drug resistance[5,6]. In recent years, a broadening range of nanomaterials has been developed to efficiently fight infections, which can kill bacteria through several mechanisms including membrane damage through physical/chemical interactions, disruption of electron transport homeostasis and the respiratory chain, and inducing bacterial oxidative stress through direct generation of reactive oxygen species (ROS) through catalytic processes[7,8]. Nevertheless, the development of drug resistance is a complicated process, and different bacterial strains exhibit varying degrees of resistance[9]. For example, compared to Gram-positive bacteria, Gram-negative bacteria usually have more specific protein pumps that pump antibiotics out of the cell[10]. So far, the antibacterial nanomaterials have shown a significant increase in bactericidal efficacy, whereas the recognition of specific bacterial strains is unsatisfactory. Therefore, specific sterilization of different strains of bacteria via multi-targeting bactericidal mechanisms is of great significance for the development of elaborated antibacterial nanomedicine[11,12]. Prevailing strategies have proven successful in targeting Gram-positive (G+) or Gram-negative (G-) bacteria in a strain-selective manner based on differences in cell membranes, such as membrane charge and sugar composition[13–15]. Another approach to achieving selective antimicrobial effect is to modify the chemical structure of the antimicrobial nanoagent, such as charge, hydrophobicity and functionality, which is also determined by the bacterial outer membrane, the primary interface between the material and the bacteria[14,16–19]. Considering that Gram-negative and positive bacteria have completely different membrane structures, we hypothesize that the binding interactions of the same antimicrobial agent with different bacterial membranes will be differing. Tang et al. have reported a series of phospholipid mimetic aggregation-induced emission luminogens (AIEgens) that selectively kill bacteria through regulating the lengths of the substituted alkyl chains of the AIEgens, which were designed based on the different structures of the two types of bacterial membranes[20]. Unfortunately, such a model of selective elimination of bacteria would deactivate the antibacterial effect on another bacterium, which is not conducive to the development of broad-spectrum nano-antimicrobials.

Thanks to their component-tunable and easily modifiable features, nanomaterials have the prospect of achieving strain-specific, multi-target, broad-spectrum bactericidal effects, which greatly facilitate the handling of antibiotic resistance[21–23]. Titanium dioxide (TiO_2)-based photocatalysts have shown promising potential in the field of antimicrobial agents thanks to their high efficiency, low cost, and biocompatibility[24–26]. In recent years, a growing number of researchers have developed many emerging titanium oxide-based antibacterial strategies. Yang et al. prepared TiO_2/TiO_{2-x} metasurfaces with potent NIR-responsive antimicrobial activity on titanium alloy implants by an alkaline–acid bidirectional hydrothermal (aaBH) method, which showed great antibacterial effect under low-power NIR irradiation[27]. However, to enhance the ability to treat infections in vivo, nanomaterials with antimicrobial capacity in dark condition are required. Li et al. reported that black titania nanotube arrays (B-TNT) on a titanium substrate had significant bactericidal capacity in dark condition by generating superoxide anions, hydroxyl radicals and singlet oxygen[28]. Therefore, it is imperative to develop new titanium oxide-based nanomaterials which possess broad-spectrum bactericidal activity without the need for external stimuli, and have a synergistic antibacterial effect with multiple bactericidal mechanisms.

Here, we present an antibacterial nanoagent ($TiO_x@C$) with both bacterial cell wall specificity and broad-spectrum bactericidal properties. The $TiO_x@C$ nanocomposite, which is composed of a carbon substrate and decorated multivalent TiO_x quantum dots, was obtained from the MXene nanomaterial (Ti_3C_2) through its self-structural evolution via facile, gentle oxidation. In such a two-in-one nanomaterial, the carbon substrate endows it with cell wall selectivity, and the TiO_x quantum dots on the surface enable an enhanced electron-donor effect. A series of in vitro experiments have revealed that $TiO_x@C$, which is unable to penetrate the bacterial membrane of *Staphylococcus aureus* (*S. aureus*) due to size effects, can selectively localize on its peptidoglycan layer and further disrupt the electron transport chain through excess electron inflow. Simultaneously, the bacterial membrane of *Pseudomonas aeruginosa* (*P. aeruginosa*) was significantly destroyed after $TiO_x@C$ treatment and resulting in severe contents leakage. It is noteworthy that the synergistic electromechanical bacterial inhibition strategy does not cause the evolution of drug resistance. In animal models of wound infection, both the bactericidal activity and the wound-healing promoting effect of $TiO_x@C$ have been demonstrated. The as-presented bacterial cell wall-specific, multi-target nanomedicine provides a distinct electron-mechanical co-intervention strategy in the personalized and effective treatment of infections, which has paved the way for emerging antibacterial nanoagents in combating drug resistant bacteria (Fig. 1).

Results and discussion

Synthesis and characterization of $TiO_x@C$

First, Ti_3C_2 nanosheets were synthesized by a chemical exfoliation method according to the previous literature[29]. In general, Ti_3C_2 nanosheets are considered to be highly sensitive to strong oxidants due to their large specific surface area, making active Ti atoms easily to be oxidized to titanium oxide[30]. Here, we treated the Ti_3C_2 aqueous dispersion with H_2O_2 to obtain the oxidation product (Fig. 2a). Transmission electron microscopy (TEM) images show the microstructure transformation of Ti_3C_2 before and after H_2O_2 oxidation (Figs. S1, Supplementary information). The final product, referred to as $TiO_x@C$, displayed a carbon layer with a silk-like structure in which TiO_x dots of 2 to 5 nm were uniformly distributed, thus forming the $TiO_x@C$ nanocomposites (Fig. 2b). The stability of $TiO_x@C$ in aqueous solution was further investigated. Digital photographs, TEM images and UV-vis spectra results show that the morphology and composition of $TiO_x@C$ in water remained unchanged for up to 30 days (Figs. S2 and S3, Supplementary information). Furthermore, $TiO_x@C$ exhibits excellent dispersion in aqueous solution, saline, and LB Broth, thereby making it a promising nanomedicine for antimicrobial therapy (Figs. S4, Supplementary information).

The corresponding lattice planes of TiO_x quantum dots are observed by high-resolution TEM (HRTEM), indicating that the lattice distortion defects are conspicuous (Fig. 2c). Energy-dispersive X-ray spectroscopy (EDS) mappings by TEM and SEM demonstrate that the Ti, O, and C elements are uniformly distributed throughout the nanohybrids, revealing that the TiO_x are evenly decorated on the carbon layer without significant aggregation (Figs. S5–6, Supplementary information). The X-ray diffraction (XRD) patterns of the precursor Ti_3C_2 and $TiO_x@C$ show that the disappearance of 2θ peak at 9.5° after the formation of $TiO_x@C$, indicating that the layered structure no longer existed (Fig. 2d)[29]. While $TiO_x@C$ shows no obvious indication of crystallinity, due to the amorphous structure of carbon layer. Raman results reveal that the characteristic peaks of Ti_3C_2 completely disappeared in the Raman spectra of $TiO_x@C$, while the different peaks at 153.9 and 623.5 cm^{-1} can be observed, which correspond to the symmetric stretching and bending vibration of O-Ti-O in Ti_3O_5 respectively (Fig. 2e)[31]. Electron paramagnetic resonance (EPR) was used to confirm the presence of oxygen vacancies (OVs). The EPR spectrum of $TiO_x@C$ displays a g value of about 2.004, confirming the presence of OVs in TiO_x (Fig. 2f)[32]. As evidence for the presence of multivalent titanium grew, X-ray photoelectron spectroscopy (XPS)

was used to verify the chemical state of TiO$_x$@C. In the Ti 2p spectrum (Fig. 2g), the characteristic peaks of Ti 2$p_{1/2}$ at 463.8 eV and Ti 2$p_{3/2}$ at 458.2 eV indicate the Ti^{3+} in TiO$_x$, and the characteristic peaks of Ti 2$p_{1/2}$ at 464.8 eV and Ti 2$p_{3/2}$ at 458.8 eV correspond to Ti^{4+}, confirming the multivalent state of Ti in TiO$_x$. The O1s spectrum shows four characteristic peaks centered at 530.0, 530.7, 531.7 and 532.6 eV, corresponding to the Ti-O bonds, hydroxylated surface, the presence of OVs and adsorbed moisture respectively, which is consistent with the EPR results (Fig. 2h). The C 1s spectrum exhibits two peaks at 284.8 and 287.5 eV, corresponding to the C-C and C-O bonds in the carbon layer, respectively (Fig. 2i)[33]. The high intensity of the C-C peak indicates the enhanced electrical conductivity of TiO$_x$@C.

To gain deeper insight into the effect of structural evolution on the performance of Ti$_3$C$_2$, first-principles DFT calculations were performed, and the optimized models were provided (Figs. S7, Supplementary information). According to the partial density of states (PDOS) calculation results, the pristine oxygen-capped Ti$_3$C$_2$ shows metalloid properties; above the Fermi level (Ef), the dominant contribution to the DOS comes from the d orbitals of Ti atoms, while below the Fermi level, the prevailing contribution to the DOS comes from the p orbitals of the O atom orbitals. Besides, the PDOS of Ti 3d of TiO$_x$ exhibits a stronger intensity around the Fermi level, thus improving conductivity and promoting the electron transfer of TiO$_x$ (Figs. S8, Supplementary information). It is typically believed that the arc radius in electrochemical impedance spectroscopy (EIS) is proportional to the resistance of the material; a smaller arc radius indicates a lower electron transport resistance in the material[34]. As shown in Figure S9, the lower electrochemical impedance of TiO$_x$@C indicates a stronger electron transport capability than Ti$_3$C$_2$.

Antibacterial performance of TiO$_x$@C

Inspired by the unique structure and improved electron-donating ability of TiO$_x$@C, the potential of TiO$_x$@C as a bactericidal agent was further investigated. *Staphylococcus aureus* (*S. aureus*), which is a major bacterial human pathogen representative of gram-positive bacteria (G +)[35], and *Pseudomonas aeruginosa* (*P. aeruginosa*) that is one of the top-listed pathogens causing hospital-acquired infections[36], representing for gram-negative bacteria (G−), were used as model bacteria. As shown in Fig. 3a–c, TiO$_x$@C exhibited broad-spectrum and concentration-dependent antibacterial activity, while the titanium-based nano-antibacterial agent Ti$_3$C$_2$ nanosheets and TiO$_2$ nanoparticles showed negligible intrinsic antibacterial performance, which depend on additional external light irradiation to generate photothermal/photodynamic therapy as previously reported[37,38]. The results suggest that the specific electronic property of TiO$_x$@C with abundant oxygen vacancies and multivalent states contributes to its antimicrobial activity. Notably, *P. aeruginosa* was more easily eradicated than *S. aureus* when the concentration of TiO$_x$@C was increased to 30 μg mL^{-1}, which highlights the potential strain-specific bactericidal mechanism of TiO$_x$@C. Confocal laser scanning microscope (CLSM) was used to observe the viability and cytotoxicity of bacteria stained by NucGreen and EthD-III. EthD-III is a cell membrane-impermeable nucleic acid dye that can determine bacteria with membrane damage. The CLSM images demonstrated the concentration-dependent antibacterial performance of TiO$_x$@C (Fig. 3d). Then, the bacterial growth inhibition effect of TiO$_x$@C was determined. The results demonstrate that TiO$_x$@C inhibited the growth of *S. aureus* by 57.3% and *P. aeruginosa* by 64.9% at a concentration of 100 μg/mL for 24 h. Therefore, the minimum inhibitory concentration that inhibits
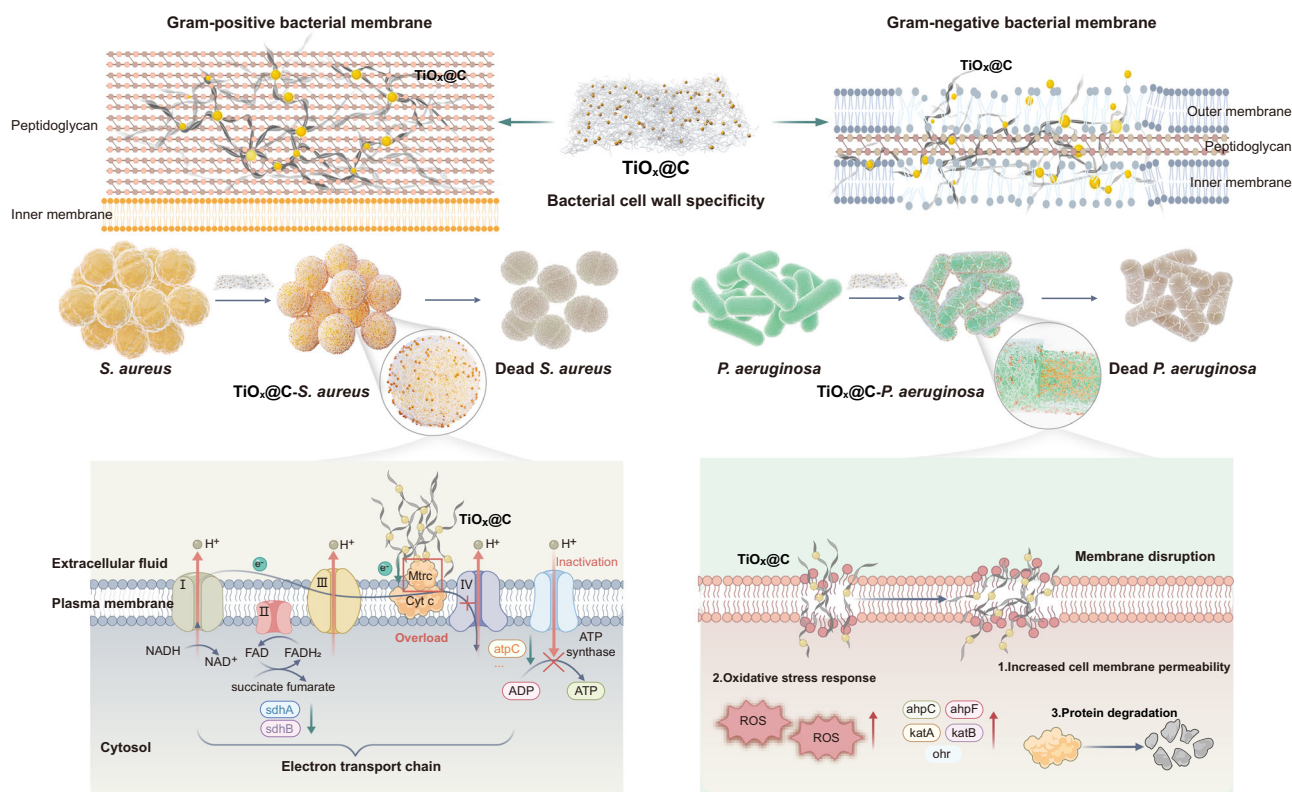
Fig. 1 | TiO$_x$@C with bacterial cell wall specificity for effective bacterial elimination through electron-mechanical intervention. The fiber-like carbon substrate of TiO$_x$@C is capable of selectively entangling with the peptidoglycan layer of *S. aureus*, further disrupting the electron transport chain and killing the bacteria by delivering excess electrons to key enzymes of the electron transport chain via

TiO$_x$ dots. Meanwhile, the carbon substrate of TiO$_x$@C could directly penetrate the cell wall of *P. aeruginosa*, disrupt the bacterial membrane structure and penetrate into the bacteria, and trigger oxidative stress and protein leakage, thus leading to the bacterial death.
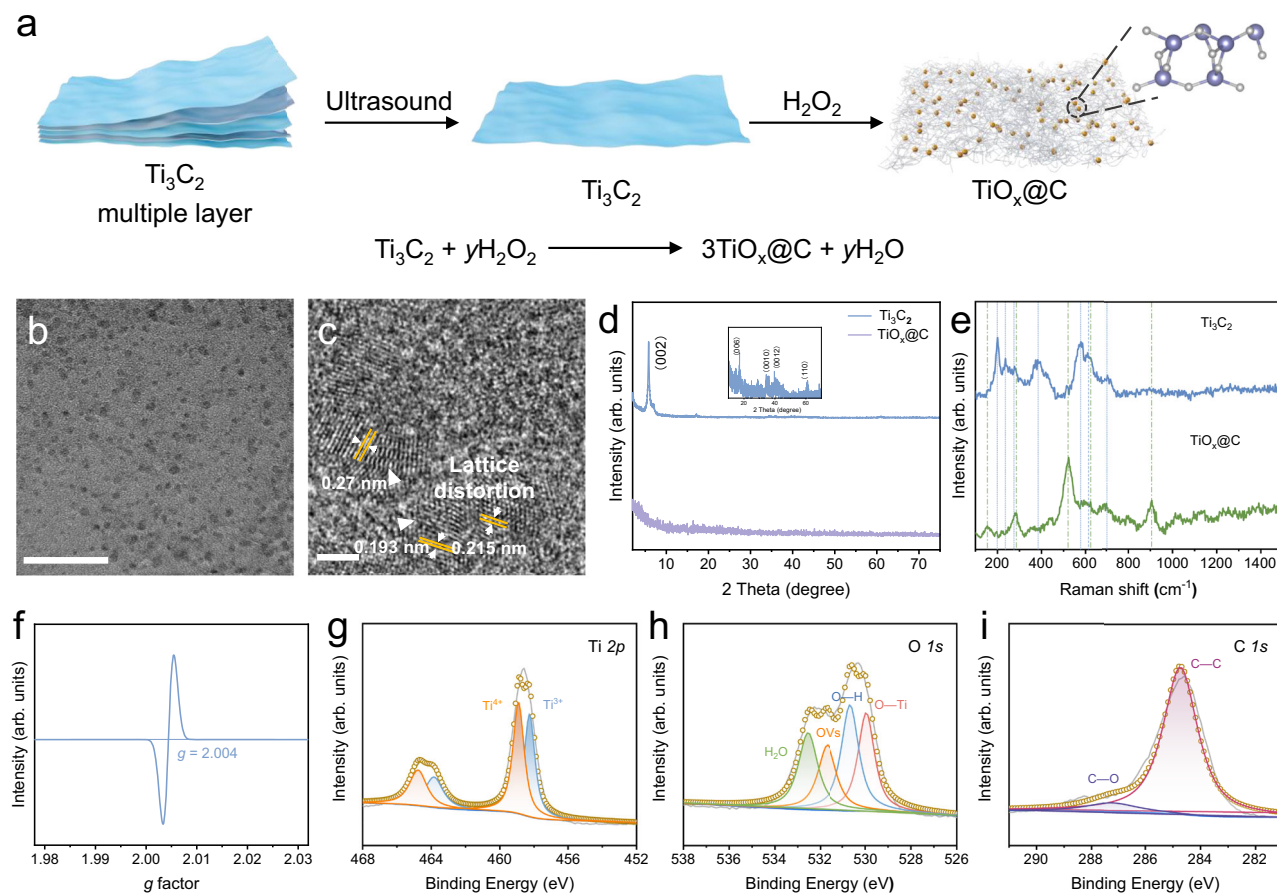
$$Ti_3C_2 + yH_2O_2 \longrightarrow 3TiO_x@C + yH_2O$$

Fig. 2 | Synthesis and characterization of TiO$_x$@C. a Schematics for the synthesis of TiO$_x$@C nanocomposite. **b** TEM images of TiO$_x$@C nanocomposites scale bar, 50 nm. **c** HRTEM image of TiO$_x$@C, scale bar, 2 nm. The white arrows indicate the lattice distortion. $n = 3$ samples with similar results. XRD pattern (**d**) and Raman spectra (**e**) of Ti$_3$C$_2$ and TiO$_x$@C. (**f**–**i**) EPR spectra (**f**) and Ti 2p (**g**), O1s (**h**), C 1s (**i**) XPS profiles of TiO$_x$@C.

50% of the bacteria (MIC50) of TiO$_x$@C for *S. aureus* and *P. aeruginosa* is 100 μg/mL (Figs. S10, Supplementary information). It can be found that TiO$_x$@C inhibited the growth of *S. aureus* by 94.2% and *P. aeruginosa* by 91.6% at a concentration of 200 μg/mL for 24 h. Therefore, the minimum inhibitory concentration that inhibits 90% of the bacteria (MIC90) of TiO$_x$@C for *S. aureus* and *P. aeruginosa* was 200 μg/mL.

Considering the accelerated evolution of bacterial AMR against antibiotics, we further evaluated whether prolonged exposure to TiO$_x$@C nanocomposites would similarly lead to the acquisition of bacterial resistance. The antibacterial efficacy of TiO$_x$@C was evaluated by screening *S. aureus* and *P. aeruginosa* strains for a period of 21 days at sub-MIC90 values[39]. The results demonstrate that TiO$_x$@C exhibited a prolonged antibacterial effect without the induction of resistance (Figs. S11 and S12, Supplementary information). A growing number of studies have revealed that nanomaterials can induce bacterial resistance through a range of mechanisms, such as Ag NPs[40], TiO$_2$ NPs[41], and CNTs[42]. It is notable that TiO$_x$@C has two components which have parallel correspondences to independent bacterial targets i.e., the bacterial cell wall, the electron transport system and redox homeostasis, which can achieve the synergy of the multiple independent bactericidal mechanisms in circumventing bacterial drug resistance[8].

Biofilms exhibit a higher prevalence of multidrug resistance to most clinically available drugs, which is a crucial issue needing to be tackled[43]. Unfortunately, extracellular polymeric substances (EPSs) bound to the cell surfaces of the biofilm can hinder the interaction of nanomaterials or drugs with the biofilm, thus reducing their germicidal efficacy[44]. Excitedly, it has been reported that boosted electron transfer between nanomaterials and bacteria can destroy the EPSs and eliminate biofilms without developing drug resistance[45]. The crystal violet method was performed to qualitatively and quantitatively evaluate the ability of TiO$_x$@C to eliminate biofilms. The results indicate that the amount of crystal violet adhered to the biofilm treated by TiO$_x$@C was significantly reduced, confirming that such material could effectively eliminate both *S. aureus* and *P. aeruginosa* biofilms (Fig. 3e). As shown in Fig. 3f, g, the quantitative results demonstrate that the anti-biofilm activity of TiO$_x$@C exhibits a concentration-dependent manner, and the elimination rate of *P. aeruginosa* biofilm could reach up to 92% at a concentration of 400 μg mL^{-1}.

Bacterial cell wall-specific performance of TiO$_x$@C

The morphological changes of the bacteria before and after co-incubation with TiO$_x$@C were observed by scanning electron microscopy (SEM). The SEM images exhibit that the initial cell walls of *S. aureus* are roughened after TiO$_x$@C treatment, indicating that *S. aureus* were wrapped on the surface by the fibrous carbon layers (marked by orange labels) (Fig. 4a). As shown in the SEM images of *P. aeruginosa*, the original smooth cell walls become shrunk and the morphology exhibit shriveled after co-incubation with TiO$_x$@C, indicating that TiO$_x$@C has led to the loss of bacterial cytoplasm, shrinkage and/or deformation of bacterial membranes of *P. aeruginosa*. The corresponding elemental mapping demonstrates that the TiO$_x$ quantum dots were distributed uniformly on the bacterial surfaces to trap and disarm bacteria (Fig. 4b). The differences between the cell wall of *S. aureus* and *P. aeruginosa* after TiO$_x$@C treatment inspire us to
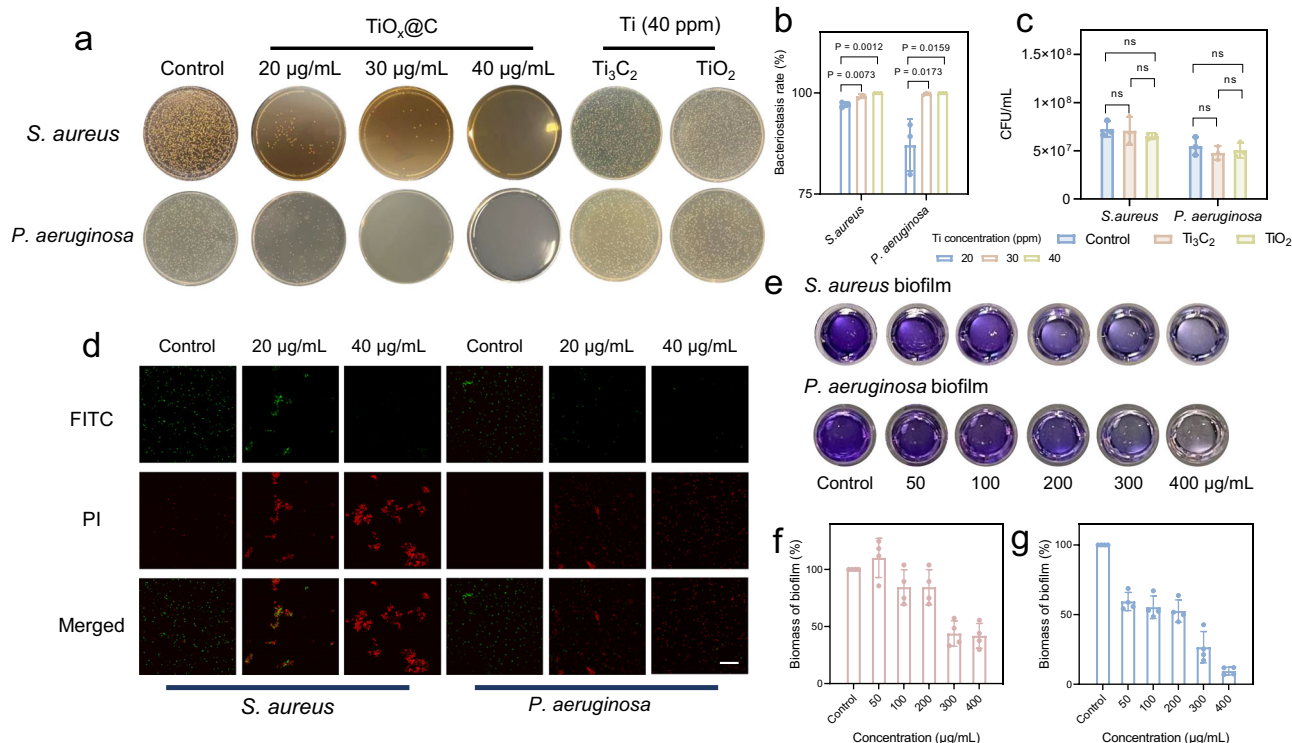
Fig. 3 | Antibacterial activity of TiO$_x$@C. a Representative optical images of *S. aureus* and *P. aeruginosa* colonies formed on LB agar plates after various treatments and (**b**, **c**) the corresponding colony counting results. *n* = 3, biological replicates. Data are presented as mean ± SD. One-way ANOVA with Bonferroni post test was used to analyze multiple groups. NS, not significant. **d** CLSM images of *S. aureus* and *P. aeruginosa* stained with NucGreen (EX488) and EthD-III /PI (EX532)

after different treatments, scale bar, 40 μm. Green color indicates live bacteria, and red color indicates membrane-damaged bacteria. n = 3, biological replicates with similar results. **e** Representative optical images of biofilms stained by crystal violet after the treatment by TiO$_x$@C at varied concentrations. (**f**, **g**) The corresponding quantitative results of *S. aureus* biofilm (**f**) and *P. aeruginosa* (**g**) biofilm. *n* = 4, biological replicates. Data are presented as mean ± SD.

investigate its potential bacterial cell wall -specific antibacterial mechanism.

Given the above hypotheses of the potential bacterial cell wall-specific antibacterial activity of TiO$_x$@C, the intrinsic antibacterial mechanisms were further investigated. Atomic force microscopy (AFM) is a powerful tool for obtaining in-depth understanding of microbial morphology and structural details[46]. The AFM results show that the smooth surface of *S. aureus* became rough after TiO$_x$@C treatment, and the corresponding root mean square roughness (Rq) increased significantly, which was consistent with the SEM results, implying that TiO$_x$@C nanomaterials were extensively attached to the surface of the *S. aureus* bacterium (Figs. S13a, Supplementary information). In contrast, the surface roughness of *P. aeruginosa* did not change significantly, instead, the thickness of the bacterium is markedly reduced (Figure S13b, Supplementary information). The three-dimensional morphology-reconstructed images intuitively reflect the deflation and indentation of the bacteria after TiO$_x$@C treatment, due to the leakage of bacterial contents (Figs. S14, Supplementary information). Bio-TEM observation was performed to further visualize the details of the internal structure of microbial cells after exposure to TiO$_x$@C, and localize the position of TiO$_x$@C within different bacteria. It can be observed that the TiO$_x$@C adhere uniformly and tightly attached to the surface of individual *S. aureus* bacteria, showing minimal ultrastructural and morphological changes. The elemental mapping images more intuitively exhibit that the carbon networks of TiO$_x$@C were entangled with the peptidoglycan (the major component of G+ cell wall) and close to the surface of the *S. aureus* inner membrane due to the outer thick peptidoglycan layer of G+ bacterium (approximately 20 ~ 40 nm), thus the carbon networks were blocked to get into the phospholipid bilayer of the bacterial inner membrane due to the size effect (Fig. 4c)[47,48].

In contrast, *P. aeruginosa* with a much thinner peptidoglycan layer (~3 nm) treated with TiO$_x$@C displayed significant morphological changes, including disruption of the cell wall, areas of clear cytoplasm, leakage of cytoplasm, and plasmolysis. In *P. aeruginosa*, the hydrophobicity and polarity of lipopolysaccharides (LPS) of its cell envelope drastically reduce the membrane permeability[49]. It has been widely reported that nanomaterials with unique morphology such as nano-wire or nanorods can cause mechanical damage by disrupting the bacterial cell membrane or cell wall, which in turn kills the bacteria[50–52]. However, such mechanical damage largely depends on the angle of interaction of material with bacteria, which greatly limits in vivo applications. In our work, The elemental mapping results show a uniform distribution of Ti element on the bacteria, suggesting the carbon network of TiO$_x$@C enables to penetrate the bacterial envelope and further enter the bacterium due to the strong hydrophobic interactions between the large number of C-C bonds, finally disrupting the bacterial membrane significantly (Fig. 4d)[53]. The interaction between TiO$_x$@C and bacterial membrane can be further confirmed by detecting the permeability of the bacterial membrane using o-nitro-phenyl-β-D-galactopyranoside (ONPG). As a result, the permeability of the bacterial membrane of *P. aeruginosa* elevated significantly with increasing concentration and prolonging incubation time after exposure to TiO$_x$@C (Fig. 4f), while those of *S. aureus* showed negligible change (Fig. 4e).

Next, the detailed changes after TiO$_x$@C treatment of the cell envelope were further elucidated at the micro/nanoscale by small angle X-ray scattering (SAXS). The exhibited SAXS profile can be divided into three regions: Region I represents the overall size of the bacterial cell in the system, including the core-shell structure. Region II contains information about the cell wall and its thickness, while region III reveals the structural arrangement of groups of objects (e.g., DNA,
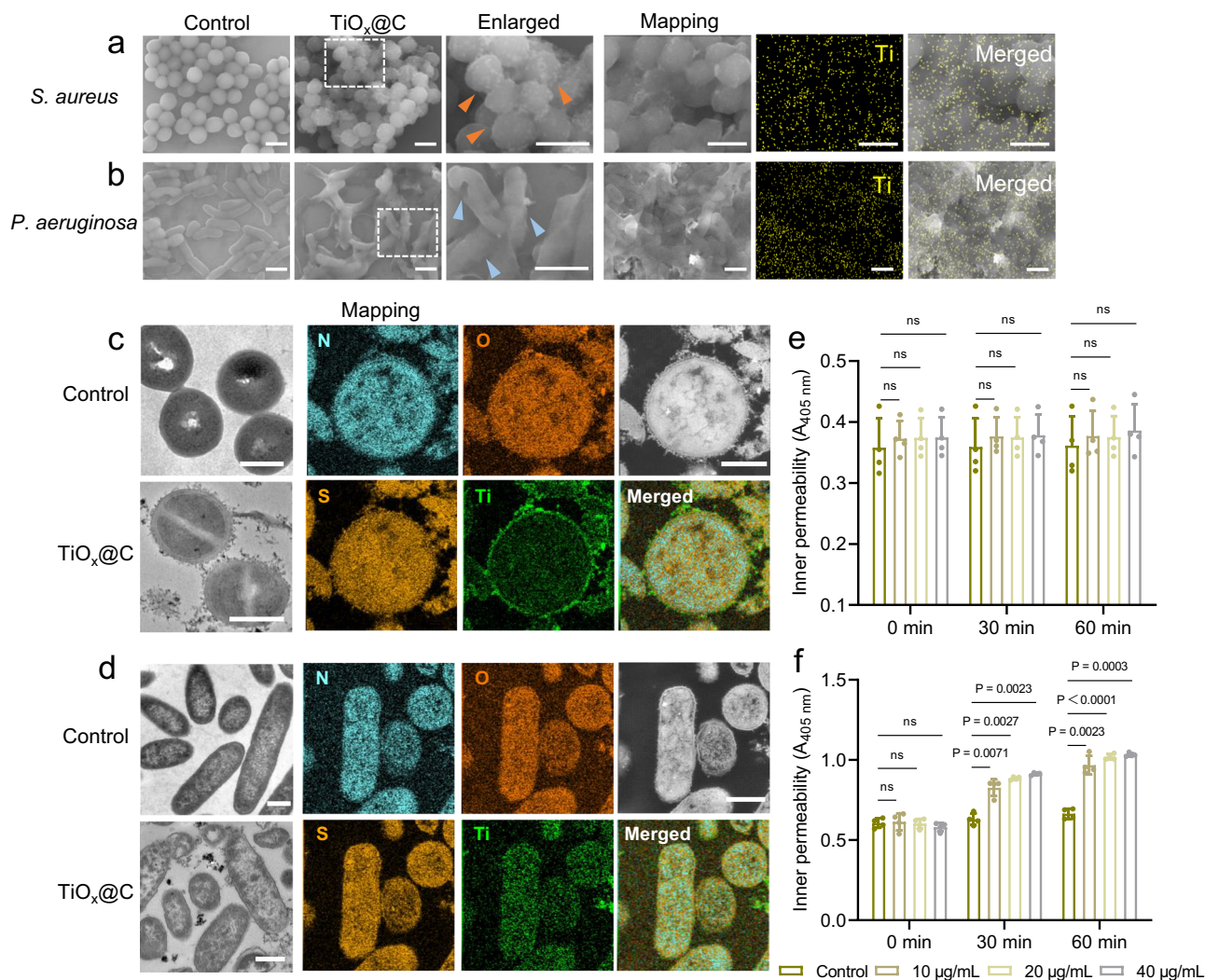
Fig. 4 | Bacterial cell wall-specific performance of TiO$_x$@C. a, b SEM images and elemental mapping of *S. aureus* (**a**) and *P. aeruginosa* (**b**) after various treatments, scale bar, 1 µm. *n* = 3, biological replicates with similar results. **c, d** Bio-TEM images and elemental mapping of *S. aureus* (**c**) and *P. aeruginosa* (**d**) before and after TiO$_x$@C treatment, scale bar, 500 nm. *n* = 3, biological replicates with similar results. **e, f** Permeability of bacterial membrane determined by ONPG assay and protein leakage analysis of *S. aureus* (**e**) and *P. aeruginosa* (**f**) after various treatments. *n* = 4, biological replicates. Data are presented as mean ± SD. Two-way ANOVA with Bonferroni post test was used to analyze multiple groups. NS, not significant.

ribosomes, and proteins) in the cytoplasm[54]. As a result, the scattering curves of TiO$_x$@C-treated *S. aureus* shifted to higher q values in region I and to lower values in region II and III, suggesting that the overall structure of the bacteria has become larger and looser, while the thinning of the bacterial wall may be accompanied by denaturation and loss of contents of the bacterial cytoplasm (Fig. 5a). On the contrary, the scattering curves of treated *P. aeruginosa* shifted toward lower q values in regions II and III, which implies that the membrane structure and cytoplasmic contents of the bacteria were significantly disrupted (Fig. 5b). Meanwhile, the protein leakage of bacteria was determined by BCA Protein Assay Kit. It could be found that the *P. aeruginosa* individuals suffered membrane damage with a decrease in total protein amount, which indicates the significant protein degradation (Fig. 5c, d).

In summary, the same antimicrobial agent would have varied binding interactions with different bacterial cell wall due to the size effect, which may lead to various antibacterial mechanisms against different bacteria. In the case of *S. aureus*, TiO$_x$@C can merely be enriched in its much thicker peptidoglycan layer owing to the large sizes of carbon substrate. Thus, few of them could disrupt the inner membrane. For *P. aeruginosa*, TiO$_x$@C is able to penetrate its

lipopolysaccharide layer and the outer membrane due to hydrophobic interaction and further disrupts the thinner peptidoglycan layer to enter the bacteria, which is directly and strongly toxic to the bacteria (Fig. 5e).

Self-driven electron transfer in bacteria-TiO$_x$@C interface

Compared to previous bacterial wall-specific antimicrobials[15–17], TiO$_x$@C was unable to enter *S. aureus* but still showed great bactericidal activity. As is known in literature, the electron transport chain (ETC) on the bacterial inner membrane plays a key role in physiological processes of bacteria such as metabolism and energy supply[55]. In recent years, interference/disruption of the bacterial electron transport chain has been applied as an emerging antibacterial strategy in a number of studies[6,8]. However, most of these are based on piezoelectric materials to achieve electron transport which require additional ultrasonic stimulation. Considering the unique electronic structure of TiO$_x$, we further explored the potential self-driven electron transport in bacteria-TiO$_x$ interface. To investigate the electrochemical activity of the TiO$_x$@C-bacteria systems, the cyclic voltammetry (CV) experiment was performed. As a result, the CV curves of *S. aureus*-TiO$_x$@C exhibit a greatly increased current signal
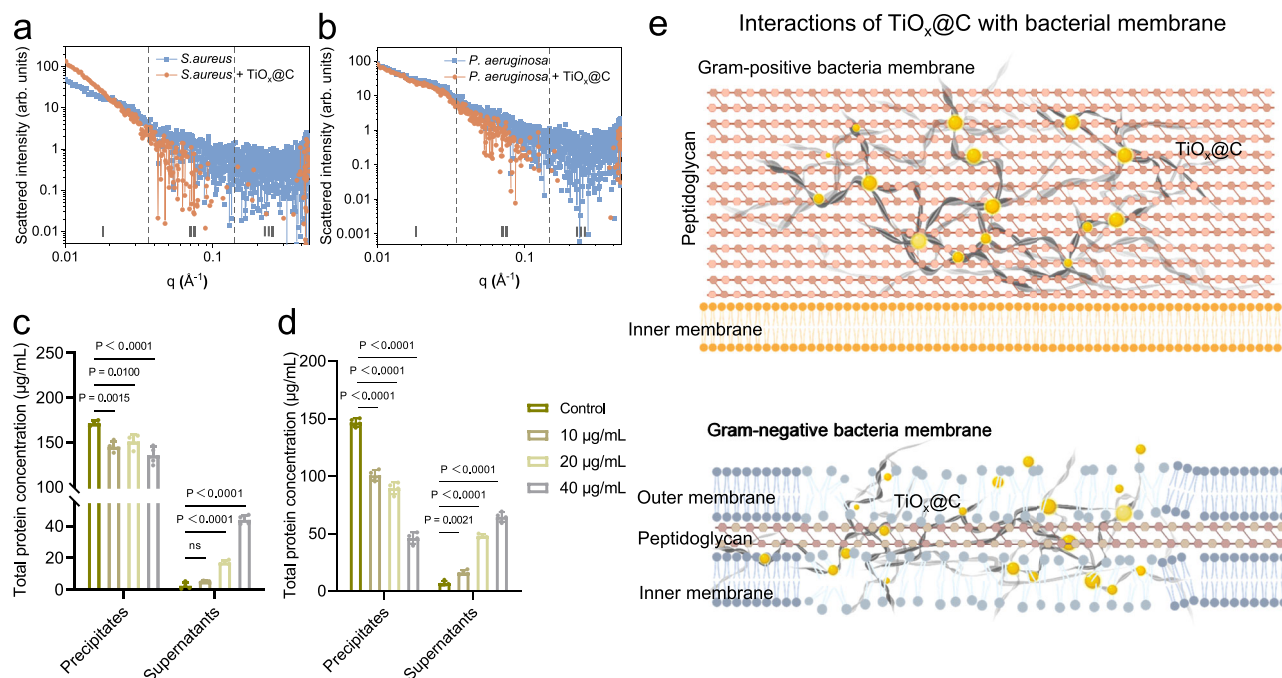
Fig. 5 | Interactions of TiO$_x$@C with bacterial membrane. a, b SAXS scattering profile for the dispersions of *S. aureus* (**a**) and *P. aeruginosa* (**b**) before and after TiO$_x$@C treatment. **c, d** Protein leakage analysis of *S. aureus* (**c**) and *P. aeruginosa* (**d**) after various treatments. **e** The corresponding schematic illustrations of interactions of TiO$_x$@C with Gram-positive or Gram-negative bacterial membrane. $n = 4$, biological replicates. Data are presented as mean ± SD. One-way ANOVA with Bonferroni post test was used to analyze multiple groups. NS not significant.

compared to untreated bacteria, while the CV curves of *P. aeruginosa* show negligible change before and after TiO$_x$@C treatment (Fig. 6a). Subsequently, electrochemical impedance spectroscopy (EIS) was used to evaluate the ability of TiO$_x$@C to boost electron transport capacity. As shown in Fig. 6b, the semicircle diameter (Rct) of the *S. aureus*-TiO$_x$@C was significantly smaller than that of untreated *S. aureus*, indicating that the TiO$_x$@C facilitates electron transfer, thus increasing the electrical conductivity of the *S. aureus*-TiO$_x$@C systems. Similarly, no significant difference was found in the EIS profiles of *P. aeruginosa* before and after TiO$_x$@C treatment.

It has been reported that nanocatalysts with similar TiO$_x$ structure exhibited efficient Fenton-like catalytic performance attributed to the abundance of surface defects and the presence of multivalent titanium[56]. The TiO$_x$@C-mediated Fenton-like reaction was evaluated using a colorimetric method based on the degradation of methylene blue (MB) after selective ·OH trapping. It can be found that the MB absorption showed a significant decay after TiO$_x$@C + H$_2$O$_2$ treatment, suggesting the production of ·OH radicals (Figs. S15, Supplementary information). Thus, we further measured the ROS levels of bacteria after TiO$_x$@C treatment. The results indicate that the bacteria in the control group emitted negligible green fluorescence, while a concentration-dependent enhancement of fluorescence emission was observed in the TiO$_x$@C-treated bacteria, possibly due to the excess ROS attack via a Fenton-like catalytic reaction[57]. (Figs. S16, Supplementary information).

Next, 2-para-(iodophenyl)-3(nitrophenyl)-5(phenyl)tetrazolium chloride (INT) was applied to detect the activity of the electron transport system (ETS). INT is a readily reducible reagent with its yellow color, which can accept hydrogen and electrons and be reduced to iodonitrotetrazolium formazan (INTF) turning purple; the rate of H$^+$/e$^-$ transfer in the ETS can be quantified by the change in absorbance. The corresponding results demonstrate an increase of absorbance at 485 nm of *S. aureus*-TiO$_x$@C system after addition of the INT detector. However, after prolonged co-incubation with TiO$_x$@C, the absorbance decreased significantly. It can be found that TiO$_x$@C is able to

temporarily enhance the electron transport activity of *S. aureus*, which is attributed to the electronic property of TiO$_x$ and the superior electrical conductivity of carbon substrate to boost electron transport capacity in a short period of time, while the electronic activity was strongly inhibited upon prolonged incubation due to abnormal electron stacking (Fig. 6c). As to *P. aeruginosa*, a marked enhancement of ETS activity was observed over a short period, which could be attributed to two aspects. On the one hand, the ETS activity was improved by TiO$_x$@C via boosted electron transport performance, and on the other hand, it may be related to the cell membrane disruption of *P. aeruginosa*, allowing more reductase enzymes in the bacterium to reduce INT. Notably, the decrease of *U*-values within 20 min of *P. aeruginosa* was greater than that of *S. aureus*, which indicates that *P. aeruginosa* suffers a mass death more quickly, corresponding to the results of the above experiments (Fig. 6d).

We then determined the stability of TiO$_x$@C before and after exerting antimicrobial effects using XPS and MB degradation tests. The results show that the valence states of Ti in TiO$_x$@C before and after co-incubation with *S. aureus* and *P. aeruginosa* has no significant changes, as the presence of carbon substrate is of great importance for maintaining the titanium in a relatively stable valence state or metastable state (Fig. S17, Supplementary information). And TiO$_x$@C still exhibited significant Fenton-like activity after co-incubation with bacteria (Fig. S18, Supplementary information), suggesting that TiO$_x$@C is able to inhibit bacterial growth efficiently over a long period of time. Moreover, the microbial ATP synthase concentration of the bacteria after various treatments was determined by enzyme linked immunosorbent assay (ELISA). The results indicate that the ATPase level of both *S. aureus* and *P. aeruginosa* decreased significantly after co-incubation with TiO$_x$@C (Fig. 6e, f). The ATPase activity of *S. aureus* decreased more rapidly in a short period of time due to the direct damage to the ATPase by the TiO$_x$@C anchored on the bacterial membrane. Simultaneously, the adenosine triphosphate (ATP) levels of bacteria show the same trend as the decreased ATP synthase activity, indicating that the inhibition of the bacterial electron
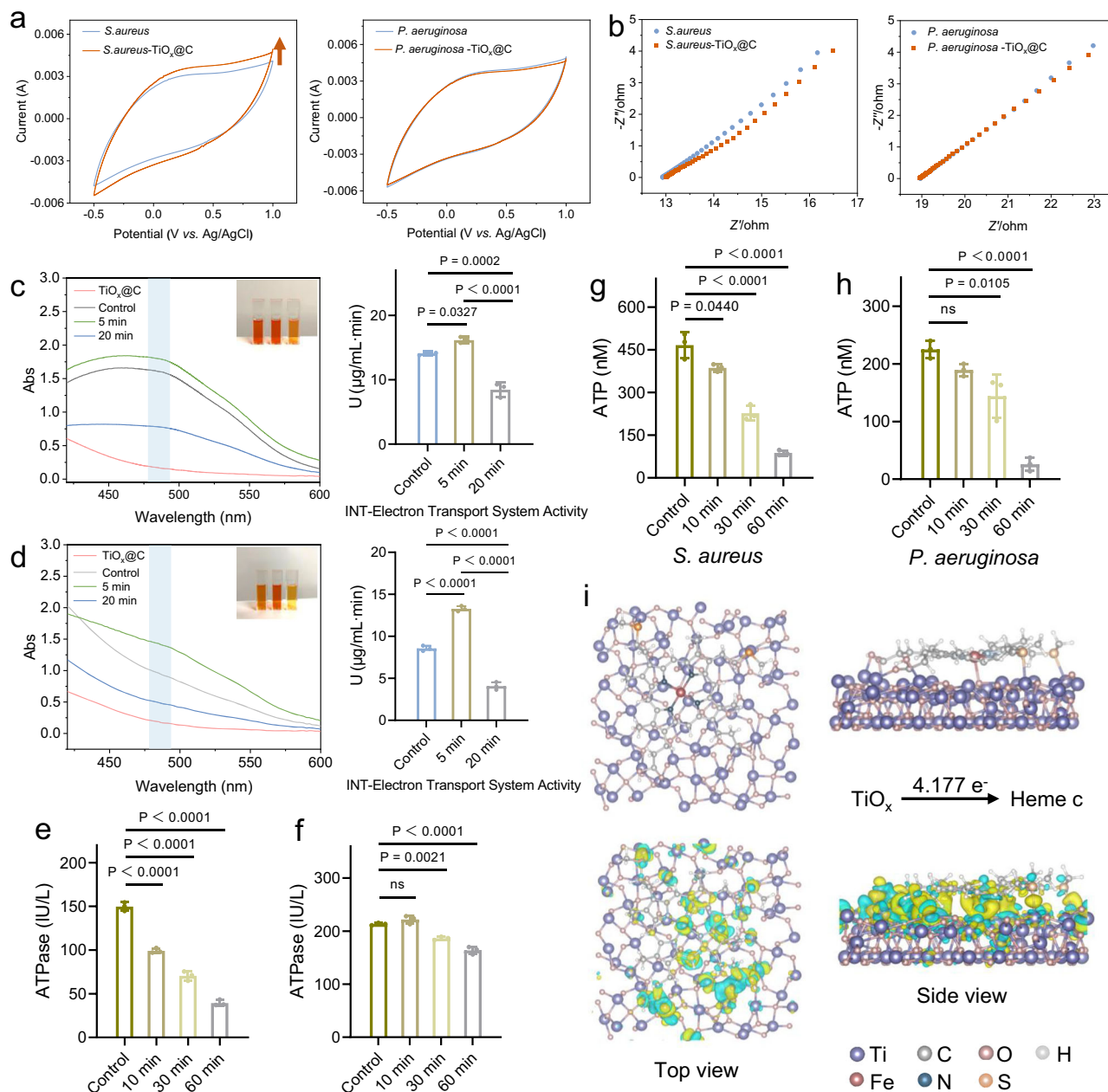
Fig. 6 | Electron transfer between bacteria and TiO$_x$@C. a Cyclic voltammetry (CV) curves of suspended *S. aureus* and *P. aeruginosa* after various treatments. **b** EIS spectrum of suspended *S. aureus* and *P. aeruginosa* after various treatments. **c, d** The corresponding INT-ETS assay outcomes containing UV-vis spectrum and quantitative ETS results of *S. aureus* (**c**) and *P. aeruginosa* (**d**) after various treatments. $n = 3$, biological replicates. Data are presented as mean ± SD. One-way ANOVA with Bonferroni post test was used to analyze multiple groups. (**e, f**) The ATPase concentration of *S. aureus* (**e**) and *P. aeruginosa* (**f**) treated with TiO$_x$@C. $n = 3$, biological replicates. Data are presented as mean ± SD. One-way ANOVA with Bonferroni post test was used to analyze multiple groups. NS, not significant. (**g, h**) The ATP level of *S. aureus* (**g**) and *P. aeruginosa* (**h**) treated with TiO$_x$@C. $n = 3$, biological replicates. Data are presented as mean ± SD. One-way ANOVA with Bonferroni post test was used to analyze multiple groups. NS, not significant. (**i**) Structural optimization of heme c adsorption on TiO$_x$@C and electron density difference plots at the heme c and TiO$_x$@C interface from top view and side view.

transport chain leads to insufficient motive force of the proton pump to enable ATP synthesis, resulting in a decrease in ATP levels (Fig. 6g, h).

Cytochrome c (cyt c) consisting of numerous heme c groups, an iron-containing biomolecule, plays a crucial role in the electron transport chain of bacteria, which facilitates the ordered transfer of electrons within the cell through its structural domains with iron-copper centers[58]. Therefore, we simulated the electron flow between heme c and TiO$_x$@C. The electron accumulation and depletion regions are presented as yellow and blue areas respectively. Notably, the redistribution of electrons occurs at the interface between heme c and

TiO$_x$@C. The electron flow (e$^-$) values of TiO$_x$@C to heme c were further elucidated by Bader charge analysis (Fig. S19, Supplementary information). Consequently, a large accumulation of electrons occurred in the heme (iron center) structural domain, which is critical for heme c (Fig. 6i). The results demonstrate that TiO$_x$@C is capable of overloading heme c with electrons and further inactivating cyt c activity, disrupting the bacterial electron transport chain and inducing bacterial death.

In summary, TiO$_x$@C exhibits a synergistic electronic-mechanical bactericidal effect. For *P. aeruginosa*, TiO$_x$@C can directly penetrate the bacterial membrane and cause severe mechanical damage. For

S. aureus, TiO$_x$@C is unable to directly damage the bacterial membrane, but can adhere to the bacterial membrane and disrupt the bacterial electron transport chain.

Specialized antibacterial mechanisms of TiO$_x$@C against *S. aureus* and *P. aeruginosa*

Further, we performed a transcriptomic analysis on *S. aureus* and *P. aeruginosa* samples to investigate the effects of the membrane interaction-guided electron-mechanical intervention of TiO$_x$@C against bacteria on gene expression and regulation. Preliminary identification of differentially expressed genes (DEGs) between the normal bacteria group and the TiO$_x$@C-treated group was performed. The volcano plot shows that the TiO$_x$@C-treated group had 968 DEGs compared to the untreated normal *S. aureus* (Fig. 7a).

Gene Ontology (GO) enrichment analysis reveals that DEGs in the *S. aureus* groups were involved in biological processes, cellular components and molecular functions especially in structural constitution of ribosome, extracellular region and translation, indicating that TiO$_x$@C induced a stress response (Fig. 7b). It is noted that DEGs involved in electron carrier activity and ATP synthase activity were significantly down-regulated in *S. aureus* after TiO$_x$@C treatment, which is consistent with the experimental results. Kyoto Encyclopedia of Genes and Genomes (KEGG) enrichment analysis shows that photosynthesis pathway involving proton motive and reducing forces and ATP synthase, was the most differentially expressed in *S. aureus* treated with TiO$_x$@C (Figs. S20a, Supplementary information). And the corresponding eight genes involved in this pathway which are genetically associated with the composition and activity of the FoF$_1$-ATPase were significantly down-regulated (Fig. S21, Supplementary information), demonstrating that the antibacterial mechanism of TiO$_x$@C against *S. aureus* is to disrupt ATP synthase activity and interfere with the energy metabolism of the bacteria. Expression heat maps disclose that the expression of succinate dehydrogenase (SDH)-related genes such as sdhA (representing flavoprotein subunit) and sdhB (representing iron-sulfur protein subunit) was downregulated, demonstrating the efficacy of TiO$_x$@C in disrupting the electron transport chain of *S. aureus*, thus suppressing its respiratory chain (Fig. 7c)[59]. Moreover, the expression of the atpC gene, which encodes the γ subunit of the ATP synthase F1 complex that plays a pivotal role in cellular respiration in bacteria and energy supply system was significantly downregulated in the TiO$_x$@C-treated group[60]. The chordal diagram depicting the enriched GO pathways of the DEGs exhibits that downregulation of key genes implies the disruption of bacterial ETCs due to blocked ATP synthesis and energy depletion. leading to *S. aureus* death (Fig. 7d). Cluster of homologous genes (COG) analysis is a common technique for microbial genome annotation and comparative genomics. The COG results indicated that genes related to translation, ribosomal structure and cell wall/membrane/envelope biogenesis were significantly downregulated, reflecting those physiological metabolic processes, such as cell wall structure, RNA transcription and protein synthesis were significantly suppressed in the bacteria after TiO$_x$@C treatment (Figure S22a, Supplementary information).

Taken together, the antibacterial mechanisms of TiO$_x$@C against gram-positive bacteria could be summarized as follows: Owing to the size effect, the fiber-like carbon substrate of TiO$_x$@C entangles with peptidoglycan layer of *S. aureus*, which allows direct interface with the electron transport chain complexes on the cell membrane. Then, TiO$_x$ quantum dots with enhanced electron-donating ability exert electron flow into crucial enzymes of the ETC leading to electron stacking which disrupts the bacterial electron homeostasis. As a result, the damaged electron transport chain is unable to form the proton gradient for ATP synthesis. This disrupts bacterial metabolism and ultimately induces bacterial death (Fig. 7e).
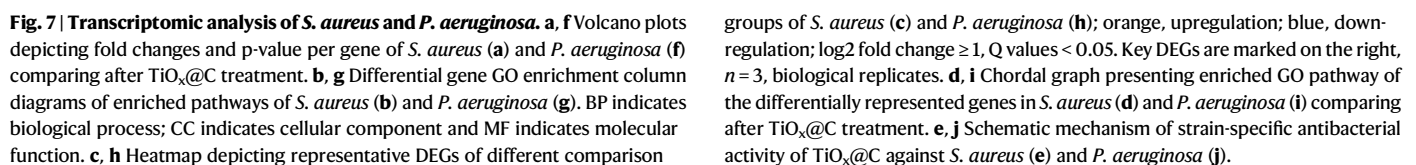
The DEGs of *P. aeruginosa* differed significantly from those of *S. aureus*. In terms of *P. aeruginosa*, the treated group showed only 89 DEGs compared to the normal group (Fig. 7f). Specifically, GO enrichment analysis demonstrates that the oxidative stress response is of most differential expression in TiO$_x$@C-treated bacteria, suggesting that TiO$_x$@C induces oxidative stress in *P. aeruginosa*, which is consistent with the flow cytometry results (Fig. 7g). KEGG analysis results show that important pathways such as glyoxylate and dicarboxylate metabolism output and lipopolysaccharide biosynthesis were enriched in TiO$_x$@C-treated *P. aeruginosa*, revealing that TiO$_x$@C induces a stress response in bacteria to generate adaptation to environmental changes (Figs. S20b, Supplementary information). Moreover, several genes related to oxidative stress and bacterial redox homeostasis were significantly upregulated (Fig. 7h). The chordal diagram depicting enriched GO pathways of the 6 representative DEGs exhibits that the upregulation of ahpC (known as alkyl hydroperoxide reductase subunit C), ahpF (known as alkyl hydroperoxide reductase subunit F), katA and katB (encode for the enzyme catalase). In detail, the katB indicates that the bacteria have been damaged by oxidative stress, resulting in the upregulation of important enzymes involved in the detoxification of reactive oxygen species (Fig. 7i). The COG results indicated that genes related to the inorganic ion transport and metabolism which is largely related to the synthesis of oxidative stress-related enzyme were upregulated, verifying that *P. aeruginosa* suffered from oxidative stress after treatment with TiO$_x$@C (Figure S22b, Supplementary information).

To sum up, the antibacterial mechanism of TiO$_x$@C against Gram-negative bacteria can be summarized as follows: Due to the hydrophobic effect, the fibrous carbon substrate of TiO$_x$@C can penetrate the outer and inner phospholipid bilayers of Gram-negative bacteria, further disrupting the bacterial membrane structure and altering membrane permeability. Then, TiO$_x$ quantum dots with unique electronic property introduce electron flow to macromolecules, proteins, metabolic enzymes in the bacterial cytoplasm to disrupt redox homeostasis, inducing bacterial oxidative stress. Finally, the membrane of Gram-negative bacteria is destroyed, resulting in severe oxidative stress damage and significant protein degradation and loss, which ends up in bacterial death (Fig. 7j).

Treatment of wound infection in vivo. Biocompatibility is of great significance for the development and application of biomedical nanomaterials. Thus, we investigated the cytotoxicity of TiO$_x$@C using the Cell Counting Kit-8 (CCK-8) assay. The results demonstrate that TiO$_x$@C shows negligible cytotoxicity to PC12 and L929 cells even when the concentration was up to 300 μg mL^{-1} (Figs. S23, Supplementary information). In addition, for further biological applications, we verified the biosafety of TiO$_x$@C to human cells. CCK-8 assay demonstrate the biocompatibility of TiO$_x$@C to HacaT cells (Human Keratinocytes cells) (Figs. S24, Supplementary information). Considering the ability of TiO$_x$@C to disrupt bacterial membranes, we further investigated the membrane integrity of the cells after co-incubation with the material. By staining the cells with PI dye, which is able to penetrate damaged cell membranes, it can be found that the cell membrane of HacaT cells incubated with TiO$_x$@C was not disrupted (Figure S25, Supplementary information). The results suggest that TiO$_x$@C is unable to penetrate the cell membrane of eukaryotic cells, due to differences in the composition of bacterial and eukaryotic cell membranes. It is well known that cholesterol (Chol), which regulates the bending rigidity of cell membranes is uniquely linked to cell evolution−it is universally absent in prokaryotic membranes and is present in differing amounts in eukaryotic membranes. The differential nature of the cell membrane serves as a barrier to prevent the carbon substrate from disrupting the integrity of the mammalian cell membrane, thus enabling microbial selectivity.

Inspired by the effective, multi-target antibacterial mechanism of TiO$_x$@C, we constructed a *S. aureus*-infected wound infection model to assess the in vivo therapeutic efficacy. The in vivo experimental

Fig. 7 | Transcriptomic analysis of *S. aureus* and *P. aeruginosa*. a, f Volcano plots depicting fold changes and p-value per gene of *S. aureus* (**a**) and *P. aeruginosa* (**f**) comparing after TiO$_x$@C treatment. **b, g** Differential gene GO enrichment column diagrams of enriched pathways of *S. aureus* (**b**) and *P. aeruginosa* (**g**). BP indicates biological process; CC indicates cellular component and MF indicates molecular function. **c, h** Heatmap depicting representative DEGs of different comparison groups of *S. aureus* (**c**) and *P. aeruginosa* (**h**); orange, upregulation; blue, down-regulation; log2 fold change ≥ 1, Q values < 0.05. Key DEGs are marked on the right, $n = 3$, biological replicates. **d, i** Chordal graph presenting enriched GO pathway of the differentially represented genes in *S. aureus* (**d**) and *P. aeruginosa* (**i**) comparing after TiO$_x$@C treatment. **e, j** Schematic mechanism of strain-specific antibacterial activity of TiO$_x$@C against *S. aureus* (**e**) and *P. aeruginosa* (**j**).

protocol is shown in Fig. 8a. As shown in Fig. 8b, c, the number of bacteria remaining in the infected lesions decreased significantly after treatments with TiO$_x$@C. The quantitative results of plate counting demonstrated that the TiO$_x$@C nanocomposites effectively eliminated 97% of the bacteria in the wounds, indicating that TiO$_x$@C is promising as a potent antimicrobial agent for the treatment of wound infections. Also, the amounts of inflammatory cells in the peripheral blood of treated mice in response to infection were mostly close to normal levels, which demonstrates that TiO$_x$@C can effectively alleviate infection-induced inflammation in vivo (Fig. 8d). Furthermore, no significant suppuration, edema and lesion expansion could be observed in TiO$_x$@C-treated group, and the wounds were able to form scabs and heal faster within two weeks in comparison to the infected (untreated) group (Fig. 8e). The schematic morphological changes of the wounds in different groups over the 14-day course display the rapid wound healing in the TiO$_x$@C -treated group, and such a rate of healing was comparable to that of the uninfected (Control) group (Fig. 8f), as evidenced by the time-dependent curves of wound areas (Figure S26a, Supplementary information). After wound modeling, all groups of mice exhibited a transient weight loss followed by an increase in body weight during the 14-day recovery monitoring period, during which the TiO$_x$@C-treated and control groups showed a
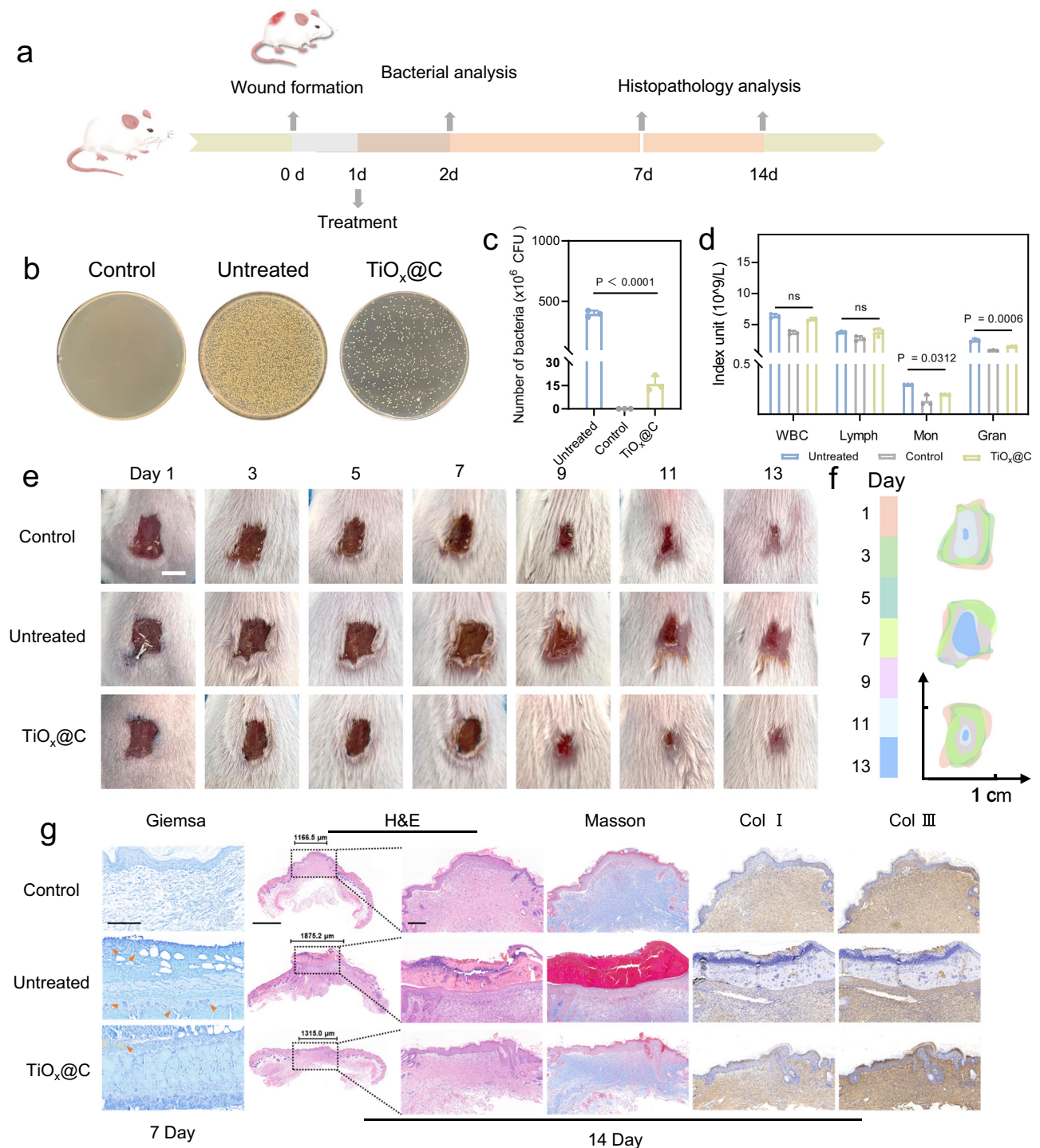
Fig. 8 | Treatment of *S. aureus*-infected wounds. (**a**) Scheme of the wound infection treatments. (**b**) Photographs of *S. aureus* colonies from infected tissues in 1 day post treatment. (**c**) Bacterial counting results corresponding to (**b**). $n = 3$, biological replicates. Data are presented as mean ± SD. One-way ANOVA was used to analyze multiple groups. (**d**) Inflammatory cell numbers in the blood of mice in different groups. $n = 3$, biological replicates. Data are presented as mean ± SD. One-way ANOVA with Bonferroni post test was used to analyze multiple groups. NS, not significant. **e** Representative images of *S. aureus*-infected skin wound of mice after treatments for different days. Scale bar, 5 mm. $n = 3$, biological replicates with similar results. **f** Schematic diagrams of the wound size changes corresponding to (**e**). **g** Giemsa staining images on day 7, scale bar, 100 μm. Orange arrows indicate the *S. aureus*-infected area. H&E, Masson and IHC, Collagen I and III (Col I and Col III) staining images of wound tissues after various treatments on day 14, scale bar, 200 μm. Scale bar for smaller magnifications of H&E images is 1 mm. $n = 3$, biological replicates with similar results. The muscle fibers are presented as red, and the collagen fibers are presented as blue in Masson staining images. Brown color indicates the Col I and III-positive.

comparable weight gaining rate and the infected group grew at the slowest rate (Figs. S26b, Supplementary information).

Accordingly, the remaining bacteria in the infected wound tissue could be further observed by Giemsa staining, which are negligible in the tissues on day 7 after TiO$_x$@C treatment. Pathomorphological analysis of the wound tissues on day 14 was conducted (Fig. 8g). The hematoxylin and eosin (H&E) staining results indicate that the healing wound skin tissue in the TiO$_x$@C-treated group had an intact tissue

composition and follicle regeneration, with a distinct stratum corneum on the surface. However, in the untreated group, the incomplete skin structure could be observed accompanied by a noticeable scab attached to the surface of the wound. The Masson's trichrome staining images suggest that more complete wound epithelium and the deposition of regenerated collagen fiber (stained blue) were observed in the infected wound tissue treated by TiO_x@C. Additionally, immunohistochemical (IHC) staining outcome shows markedly large Collagen type I and type III (Col I and Col III)-positive area in the healing wound skin after TiO_x@C treatment. Collagen type I is the major component of the ECM in skin and plays crucial role in the early inflammatory and proliferative phases of wound healing, which provides tensile strength to the wound and promotes tissue reconstruction. Col III, on the other hand, gives the wound elasticity and flexibility[61]. Col I has a higher tensile strength and will form more resilient scar tissue, while Col III allows for better wound recovery and is less likely to form scar. It can be found that Col III is more positive in the treatment group than in the control group, which indicates that TiO_x@C with promoting healing effect could achieve optimal tissue repair and minimize scar formation, possibly attributed to its porous fiber-like carbon substrate with good electrical conductivity.

Encouraged by the great antimicrobial and pro-wound healing properties of TiO_x@C in wound-infected mice, we then further evaluated the long-term toxicity of TiO_x@C in healthy mice to assess its potential application as an antibiotic alternative. The assessment of hematological and blood biochemical markers for mice on day 14 showed no significant abnormalities or deleterious effects in TiO_x@C-treated mice, suggesting that TiO_x@C has insignificant toxicity and can be used for further in vivo experiments (Figs. S27a, b, Supplementary information). Furthermore, histological analyzes of major organs (heart, liver, spleen, lungs and kidneys) were performed. H&E staining images show negligible histological abnormalities or pathological changes in TiO_x@C -treated mice compared to normal healthy mice (Figs. S27c, Supplementary information). In conclusion, TiO_x@C exhibits favorable biosafety and possesses the potential to be applied as an effective nanoagent for the synergistic treatment of bacterial infections and wound healing.

Discussion

In this study, a concept of bacterial cell wall-specific nanomedicine has been introduced, which can achieve multi-targeting and highly efficient elimination of both *S. aureus* and *P. aeruginosa* via electron-mechanical bactericidal mechanisms. In vitro experiments and further transcriptomic analyses reveal that TiO_x@C can be localized into the inner membrane and donate electrons to the significant enzymes of *S. aureus* electron transport chain, which disrupts the respiratory and metabolic pathways of the bacteria. Meanwhile, *P. aeruginosa* treated by TiO_x@C would suffer from cell membrane damage, oxidative stress, and protein leakage, which would eventually lead to bacterial death. In vivo experiments have demonstrated that TiO_x@C possesses greatly enhanced bactericidal activity and wound healing-promoting capacities simultaneously, which promotes fibroblast proliferation, and damaged skin rehabilitation and collagen regeneration. Therefore, such a safe and effective nano-antimicrobial agent can achieve efficient elimination of *S. aureus* and *P. aeruginosa* through synergistic electron-mechanical intervention without inducing drug resistance, which is expected to serve as a promising nanomedicine alternative to conventional antibiotics to combat difficult-to-treat bacterial infections by circumventing current mechanisms of drug resistance of bacteria.

Methods
Ethical approval
All animal experiments were under the context of the animal protocols approved by the Institutional Animal Care and Use Committee guidelines in Shanghai Tenth Peoples' Hospital, Tongji University School of Medicine (approval number: SHDSYY-2018-Z0026). All mice were kept in accordance with the policies on animal research of the National Ministry of Health. All mice used for animal experiments are female with a gentle character, and the sex of the mice does not affect the results of the experiments.

Materials
Ti_3AlC_2 powder (≥95 wt%) was purchased from XFNANO Materials Tech Co., Ltd. (Nanjing, China). Hydrofluoric acid aqueous solution (HF, ≥40 wt%), N-methylpyrrolidone (NMP, ≥99.7 wt%), ethanol (≥99.9 wt%) and hydrogen peroxide (H_2O_2, ≥30 wt%) were obtained from Adamas Reagent Chemical Co., Ltd. (Shanghai, China). Iodonitrotetrazolium chloride (INT, ≥98%) and Methylene blue (MB, ≥70%) were bought from Aladdin Scientific Co., Ltd. (Shanghai, China). Bacterial live/dead staining kits was bought from US Everbright Inc. (Suzhou, China). DCFH-DA, CCK-8, Calcein-AM/PI assay were bought from Keygen Biotech Co., Ltd. (Nanjing, China). ATP Assay Kit and Crystal Violet Staining Solution was obtained from Beyotime Biotech Co., Ltd. (Shanghai, China). Microbial ATPase ELISA kit was purchased from Hengyuan Biotechnology (Shanghai, China). Dulbecco's modified eagle's medium (DMEM, high glucose) and Roswell Park Memorial Institute (RPMI) 1640 medium were purchased from iCell Bioscience Co., Ltd. (Shanghai, China). Fetal bovine serum (FBS), PBS, and penicillin/streptomycin were obtained from Gibco (Thermo Fisher Scientific Inc., USA). All chemicals were used directly without further purification.

Synthesis of TiO_x@C.
a. **Synthesis of Ti_3C_2.** The Ti_3AlC_2 ceramic bulk was ground to a fine powder. About 10 g of the powder was immersed in 80 ml of 40% HF aqueous solution and left at room temperature for 3 days. Then collected by centrifugation (4601 g, 10 min) and washed several times with water and ethanol. The obtained Ti_3C_2 was dispersed in NMP (20 mg/mL) and sonicated in a water bath (200 W, 8 h). Afterwards, the precipitate was obtained by centrifugation (6010 g, 15 min) and freeze-dried to powder.
b. **Synthesis of TiO_x@C.** 1 mL of 3.0 wt% H_2O_2 was dropwise added into 10 mL of Ti_3C_2 suspension (1 mg/mL) under vigorous stirring at 4 °C and reacted for 12 h. The precipitated bulk Ti_3C_2 was removed by centrifugation (9390 g, 20 min) to obtain a stably dispersed TiO_x@C solution. Then TiO_x@C aqueous dispersion was obtained and powdered products can be obtained by freeze-drying.

Cells and Bacteria
Mouse Fibroblast cell line (L929 cells) (SCSP-5039), rat PC12 cells (SCSP-517) and human HacaT cells (SCSP-5091) were obtained from Cell Bank/Stem Cell Bank, Chinese Academy of Science. L929 cells were cultured in in RPMI-1640 medium containing 10% fetal bovine serum (FBS) and 1% penicillin/streptomycin. PC12 cells were cultured in DMEM high glucose medium added with 10% FBS and 1% penicillin/streptomycin. Both cells were cultured in a humidified atmosphere of 5% CO_2 at 37 °C. *Staphylococcus aureus* (*S. aureus*, ATCC6538), and *Pseudomonas aeruginosa* (*P. aeruginosa*, ATCC9027) were ordered from Guangdong Microbial Culture Collection Center. (Guangzhou, China). Bacteria were grown in Luria-Broth (LB) broth and LB agar (Beyotime Biotechnology). Biofilms were grown in 1/10 LB broth. The bacteria were cultured at 37 °C and passaged every day

Antibacterial experiments
Before the experiment, bacteria (*S. aureus, P. aeruginosa*) were incubated overnight in LB broth at 37 °C (240 rpm shaking). The bacteria in logarithmic growth period (OD600 = 0.5, 10^8 Colony Forming Units (CFU) mL^{-1}) were centrifuged (3280 g, 5 min) and resuspended in 100 μL saline. At the same time, 900 μL TiO_x@C saline dispersion at

different concentration (20, 30, 40 μg/mL) was added at 37 °C for 1 h. To explore the antibacterial performance of other Ti-based nanomaterials, the bacteria were treated with Ti_3C_2 and TiO_2 with the Ti concentration of 40 ppm under the same conditions. After incubation, the bacteria were diluted and plated on LB agar overnight at 37 °C. To quantify bacteriostasis, the number of colonies were counted.

Animals
Six-to-eight-week-old healthy female BALB/c mice were provided by SPF biotechnology co. (Beijing, China). All animals were housed under the standard conditions for seven days prior to treatment (temperature 20–25 °C, 12 h light/dark cycle, humidity of 60–70%). Animals were assigned to experimental groups randomly.

Biosafety evaluation
Ten female BALB/C mice were equally divided into two groups, then the mice of TiO_x@C group treated with TiO_x@C suspension through external application. The control group was fed normally without any treatment. For blood analysis, the blood samples were obtained from mice on day 14. Then, the mice were sacrificed after blood collection, and the major organs samples were taken for H&E staining and pathological evaluation.

S. aureus-infected wound model
30 female BALB/c mice were equally divided into three groups (Control, Untreated, TiO_x@C treatment). To establish wound model, all the mice were removed hair and excised a square cut (10 mm*10 mm appropriately) on the back. For bacterial infection, *S. aureus* suspension (OD600 = 1.0, 50 μL) was injected into the wound and dressed with plaster (Hynaut, China). After infection for 24 h, the TiO_x@C materials (50 μg/mL, 50 μL) were sprayed on the wounds. The lesions were recorded by taking photographs and measured by vernier. Some mice were killed on day 2 and the infected tissue were collected and homogenized to count the number of bacteria. For histopathological analysis, the lesioned skins were collected after sacrifice on day 14. The BALB/c mice with uninfected wound were used as negative control (group Control), and the infected mice without any treatments were regarded as positive control (group Untreated).

Statistical analysis
All the statistical data were presented as the mean ± standard deviation (SD) from at least three independent experiments. One-way/two-way analysis of variance (ANOVA) with Bonferron's significant difference post-hoc test was conducted for multiple comparisons, in which a P value of less than 0.05 was considered as significant difference.

Reporting summary
Further information on research design is available in the Nature Portfolio Reporting Summary linked to this article.

Data availability
All data underlying this study are available from the corresponding author upon request. The authors declare that all data needed to support the findings of this study are provided within the article, Supplementary information, and Source data file. The raw data of RNA-sequencing has been deposited in the China National Center for Bioinformation under the BioProject accession number PRJCA034742 (https://www.cncb.ac.cn/). Source data are provided as a Source Data file. Source data are provided with this paper.

References
1. Murray, C. J. L. et al. Global burden of bacterial antimicrobial resistance in 2019: a systematic analysis. *Lancet* **399**, 629–655 (2022).
2. Smith, W. P. J., Wucher, B. R., Nadell, C. D. & Foster, K. R. Bacterial defences: mechanisms, evolution and antimicrobial resistance. *Nat. Rev. Microbiol.* **21**, 519–534 (2023).
3. Willyard, C. The drug-resistant bacteria that pose the greatest health threats. *Nature* **543**, 15–15 (2017).
4. Balakrishnan, V. S. WHO's first global infection prevention and control report. *Lancet Infect. Dis.* **22**, 1122 (2022).
5. Gupta, A., Mumtaz, S., Li, C.-H., Hussain, I. & Rotello, V. M. Combatting antibiotic-resistant bacteria using nanomaterials. *Chem. Soc. Rev.* **48**, 415–427 (2019).
6. Makabenta, J. M. V. et al. Nanomaterial-based therapeutics for antibiotic-resistant bacterial infections. *Nat. Rev. Microbiol.* **19**, 23–36 (2021).
7. Huh, A. J. & Kwon, Y. J. Nanoantibiotics": a new paradigm for treating infectious diseases using nanomaterials in the antibiotics resistant era. *J. Controlled Release* **156**, 128–145 (2011).
8. Xie, M. et al. Antibacterial nanomaterials: mechanisms, impacts on antimicrobial resistance and design principles. *Angew. Chem. Int. Ed.* **62**, e202217345 (2023).
9. Van Acker, H., Van Dijck, P. & Coenye, T. Molecular mechanisms of antimicrobial tolerance and resistance in bacterial and fungal biofilms. *Trends Microbiol.* **22**, 326–333 (2014).
10. Darby, E. M. et al. Molecular mechanisms of antibiotic resistance revisited. *Nat. Rev. Microbiol.* **21**, 280–295 (2023).
11. Pillai, P. P., Kowalczyk, B., Kandere-Grzybowska, K., Borkowska, M. & Grzybowski, B. A. Engineering gram selectivity of mixed-charge gold nanoparticles by tuning the balance of surface charges. *Angew. Chem. Int. Ed.* **55**, 8610–8614 (2016).
12. Fang, G. et al. Differential Pd-nanocrystal facets demonstrate distinct antibacterial activity against gram-positive and gram-negative bacteria. *Nat. Commun.* **9**, 129 (2018).
13. Wang, L. et al. The density of surface coating can contribute to different antibacterial activities of gold nanoparticles. *Nano Lett.* **20**, 5036–5042 (2020).
14. Niu, J. et al. Antibody mimics as bio-orthogonal catalysts for highly selective bacterial recognition and antimicrobial therapy. *ACS Nano* **15**, 15841–15849 (2021).
15. Yuan, H. et al. Cationic conjugated polymers for discrimination of microbial pathogens. *Adv. Mater.* **26**, 4333–4338 (2014).
16. Liu, K. et al. Supramolecular photosensitizers with enhanced antibacterial efficiency. *Angew. Chem. Int. Ed.* **52**, 8285–8289 (2013).
17. Jia, H. R., Zhu, Y. X., Duan, Q. Y. & Wu, F. G. Cell surface-localized imaging and sensing. *Chem. Soc. Rev.* **50**, 6240–6277 (2021).
18. Zhu, C. et al. Multifunctional cationic poly(p-phenylene vinylene) polyelectrolytes for selective recognition, imaging, and killing of bacteria over mammalian cells. *Adv. Mater.* **23**, 4805–4810 (2011).
19. Wu, X. et al. Reactivity differences enable ROS for selective ablation of bacteria. *Angew. Chem. Int. Ed.* **61**, e202200808 (2022).
20. Wang, J., Li, J., Shen, Z., Wang, D. & Tang, B. Z. Phospholipid-mimetic aggregation-induced emission luminogens for specific elimination of gram-positive and gram-negative bacteria. *ACS Nano* **17**, 4239–4249 (2023).
21. Miller, K. P., Wang, L., Benicewicz, B. C. & Decho, A. W. Inorganic nanoparticles engineered to attack bacteria. *Chem. Soc. Rev.* **44**, 7787–7807 (2015).
22. Koo, H., Allan, R. N., Howlin, R. P., Stoodley, P. & Hall-Stoodley, L. Targeting microbial biofilms: current and prospective therapeutic strategies. *Nat. Rev. Microbiol.* **15**, 740–755 (2017).
23. Caster, J. M., Patel, A. N., Zhang, T. & Wang, A. Investigational nanomedicines in 2016: a review of nanotherapeutics currently undergoing clinical trials. *WIREs Nanomed. Nanobiotechnology* **9**, e1416 (2017).
24. Arun, J. et al. Synthesis and application of titanium dioxide photocatalysis for energy, decontamination and viral disinfection: a review. *Environ. Chem. Lett.* **21**, 339–362 (2023).

25. Kumaravel, V. et al. Antimicrobial TiO2 nanocomposite coatings for surfaces, dental and orthopaedic implants. *Chem. Eng. J.* **416**, 129071 (2021).

26. Chen, X. & Mao, S. S. Titanium dioxide nanomaterials: synthesis, properties, modifications, and applications. *Chem. Rev.* **107**, 2891–2959 (2007).

27. Yang, M. et al. NIR-responsive TiO2 biometasurfaces: toward in situ photodynamic antibacterial therapy for biomedical implants. *Adv. Mater.* **34**, 2106314 (2022).

28. Li, Z. et al. Antibacterial ability of black titania in dark: Via oxygen vacancies mediated electron transfer. *Nano Today* **50**, 101826 (2023).

29. Naguib, M. et al. Two-Dimensional Nanocrystals Produced by Exfoliation of Ti3AlC2. *Adv. Mater.* **23**, 4248–4253 (2011).

30. Ahmed, B., Anjum, D. H., Hedhili, M. N., Gogotsi, Y. & Alshareef, H. N. H2O2 assisted room temperature oxidation of Ti2C MXene for Li-ion battery anodes. *Nanoscale* **8**, 7580–7587 (2016).

31. Chen, Y. & Mao, J. Sol–gel preparation and characterization of black titanium oxides Ti2O3 and Ti3O5. *J. Mater. Sci.: Mater. Electron.* **25**, 1284–1288 (2014).

32. Luo, D. et al. Revealing the rapid electrocatalytic behavior of ultrafine amorphous defective Nb(2)O(5-x) nanocluster toward superior Li-S performance. *ACS Nano* **14**, 4849–4860 (2020).

33. Zhang, H. et al. MXene-derived TinO2n−1 quantum dots distributed on porous carbon nanosheets for stable and long-life Li–S batteries: enhanced polysulfide mediation via defect engineering. *Adv. Mater.* **33**, 2008447 (2021).

34. Wang, S. et al. Electrochemical impedance spectroscopy. *Nat. Rev. Methods Prim.* **1**, 41 (2021).

35. Lowy, F. D. Staphylococcus aureus infections. *N. Engl. J. Med.* **339**, 520–532 (1998).

36. Rossi, E. et al. Pseudomonas aeruginosa adaptation and evolution in patients with cystic fibrosis. *Nat. Rev. Microbiol.* **19**, 331–342 (2021).

37. Wang, J. et al. NIR-dependent photothermal-photodynamic synergistic antibacterial mechanism for titanium carbide nanosheets intercalated and delaminated by tetramethylammonium hydroxide. *Biomater. Adv.* **152**, 213492 (2023).

38. Wang, R. et al. Graphdiyne-modified TiO2 nanofibers with osteoinductive and enhanced photocatalytic antibacterial activities to prevent implant infection. *Nat. Commun.* **11**, 4465 (2020).

39. Ling, L. L. et al. A new antibiotic kills pathogens without detectable resistance. *Nature* **517**, 455–459 (2015).

40. Stabryla, L. M. et al. Role of bacterial motility in differential resistance mechanisms of silver nanoparticles and silver ions. *Nat. Nanotechnol.* **16**, 996–1003 (2021).

41. Qiu, Z. et al. Effects of nano-TiO2 on antibiotic resistance transfer mediated by RP4 plasmid. *Nanotoxicology* **9**, 895–904 (2015).

42. Anh Le, T. T., Thuptimdang, P., McEvoy, J. & Khan, E. Phage shock protein and gene responses of Escherichia coli exposed to carbon nanotubes. *Chemosphere* **224**, 461–469 (2019).

43. Ciofu, O., Moser, C., Jensen, P. Ø. & Høiby, N. Tolerance and resistance of microbial biofilms. *Nat. Rev. Microbiol.* **20**, 621–635 (2022).

44. Flemming, H.-C. & Wingender, J. The biofilm matrix. *Nat. Rev. Microbiol.* **8**, 623–633 (2010).

45. Shi, T. et al. Nanohole-boosted electron transport between nanomaterials and bacteria as a concept for nano–bio interactions. *Nat. Commun.* **12**, 493 (2021).

46. Dufrêne, Y. F. Towards nanomicrobiology using atomic force microscopy. *Nat. Rev. Microbiol.* **6**, 674–680 (2008).

47. Linklater, D. P. et al. Antibacterial action of nanoparticles by lethal stretching of bacterial cell membranes. *Adv. Mater.* **32**, 2005679 (2020).

48. Hayden, S. C. et al. Aggregation and interaction of cationic nanoparticles on bacterial surfaces. *J. Am. Chem. Soc.* **134**, 6920–6923 (2012).

49. Nikaido, H. Molecular basis of bacterial outer membrane permeability revisited. *Microbiol. Mol. Biol. Rev.: MMBR* **67**, 593–656 (2003).

50. Wang, G. et al. Quantifiable relationship between antibacterial efficacy and electro-mechanical intervention on nanowire arrays. *Adv. Mater.* **35**, e2212315 (2023).

51. Ivanova, E. P. et al. Bactericidal activity of black silicon. *Nat. Commun.* **4**, 2838 (2013).

52. Liu, Z. et al. Bio-inspired self-adaptive nanocomposite array: from non-antibiotic antibacterial actions to cell proliferation. *ACS Nano* **16**, 16549–16562 (2022).

53. Karunakaran, S., Pandit, S., Basu, B. & De, M. Simultaneous exfoliation and functionalization of 2H-MoS2 by thiolated surfactants: applications in enhanced antibacterial activity. *J. Am. Chem. Soc.* **140**, 12634–12644 (2018).

54. Duarte, H., Gummel, J., Robles, E., Berti, D. & Fratini, E. Ultra-/small angle x-ray scattering (USAXS/SAXS) and static light scattering (SLS) modeling as a tool to determine structural changes and effect on growth in s. epidermidis. *ACS Appl. Bio Mater.* **5**, 3703–3712 (2022).

55. Vercellino, I. & Sazanov, L. A. The assembly, regulation and function of the mitochondrial respiratory chain. *Nat. Rev. Mol. Cell Biol.* **23**, 141–161 (2022).

56. Jiang, Y. et al. In situ turning defects of exfoliated Ti(3)C(2) MXene into fenton-like catalytic active sites. *Proc. Natl Acad. Sci. USA* **120**, e2210211120 (2023).

57. Mitchell, A. M. & Silhavy, T. J. Envelope stress responses: balancing damage repair and toxicity. *Nat. Rev. Microbiol.* **17**, 417–428 (2019).

58. Brausemann, A., Zhang, L., Ilcu, L. & Einsle, O. Architecture of the membrane-bound cytochrome c heme lyase CcmF. *Nat. Chem. Biol.* **17**, 800–805 (2021).

59. Moosavi, B., Berry, E. A., Zhu, X.-L., Yang, W.-C. & Yang, G.-F. The assembly of succinate dehydrogenase: a key enzyme in bioenergetics. *Cell. Mol. Life Sci.* **76**, 4023–4042 (2019).

60. Fenoll, A., Muñoz, R., García, E. & de la Campa, A. G. Molecular basis of the optochin-sensitive phenotype of pneumococcus: characterization of the genes encoding the F0 complex of the Streptococcus pneumoniae and Streptococcus oralis H(+)-ATPases. *Mol. Microbiol.* **12**, 587–598 (1994).

61. Singh, D., Rai, V. & Agrawal, D. K. Regulation of collagen i and collagen iii in tissue injury and regeneration. *Cardiol. Cardiovascular Med.* **7**, 5–16 (2023).

Acknowledgements

Author contributions

Conceptualization: Y.Y. and H.L. Methodology: Y.Y., X.Y., J.J., Z.C., Y.X. Z., Y.C. Investigation: Y.Y. Supervision: H.L. and J.S. Writing, original draft: Y.Y. Writing—review & editing: H.L. and J.S.

Competing interests

The authors declare that they have no conflict of interest.

Additional information

Supplementary information The online version contains supplementary material available at
https://doi.org/10.1038/s41467-025-58061-5.

Correspondence and requests for materials should be addressed to Han Lin.

Peer review information *Nature Communications* thanks Xiangang Hu and the other, anonymous, reviewer(s) for their contribution to the peer review of this work. A peer review file is available.

Reprints and permissions information is available at
http://www.nature.com/reprints

Publisher's note Springer Nature remains neutral with regard to jurisdictional claims in published maps and institutional affiliations.